



Numerical simulation and experimental verification of large-sized Zr-based bulk metallic glass ring-shaped parts in casting process

Fei-long WANG¹, Qiu-hong HAO^{1,2}, Peng-fei YU¹, Yu-jing YANG³, Ming-zhen MA¹, Xin-yu ZHANG¹, Ri-ping LIU¹

1. State Key Laboratory of Metastable Materials Science and Technology,
Yanshan University, Qinhuangdao 066004, China;

2. Wuhan Hgcyber Data System Co., Ltd., Wuhan 430223, China;

3. Department of Physics, Hebei Normal University of Science and Technology, Qinhuangdao 066004, China

Received 21 January 2021; accepted 11 October 2021

Abstract: An outer ring of 29320 self-aligning roller bearing was used in an experimental study on the casting of $Zr_{41}Ti_{14}Cu_{12.5}Ni_{10}Be_{22.5}$ amorphous alloy. Numerical simulations of mold filling and solidification processes were carried out to determine the velocity fields and temperature fields of the alloy melt during mold filling process as well as the temperature fields and temperature gradient fields in the course of the solidification. According to the results, a cast with a complete shape can be obtained at 1200 °C under the condition that the cooling rate is greater than the critical cooling rate. The ring-shaped part with a thickness of 25 mm, an equivalent diameter of 22 mm, and a mass of 1.32 kg was prepared by gravity casting in a copper mold. X-ray diffraction and differential scanning calorimetry data revealed that the produced cast had the amorphous structure.

Key words: bulk metallic glasses; ring-shaped part; casting forming; numerical simulation; mold filling; solidification

1 Introduction

The discovery of ZrTiCuNiBe bulk metallic glasses (BMG) by PEKER and JOHNSON [1] (California Institute of Technology), whose critical cooling rate does not exceed 10 K/s, has put an end to the notion that amorphous alloys can exist only in the form of powders, strips, and films. Further development of BMGs enabled one to conduct a lot of basic research relying on the alloy systems [1–4], glass forming ability [5–9], crystallization kinetics [10–13], mechanical properties [14–17], fracture mechanism [18–20], deformation behavior [21–26], friction [27–29], fatigue [30] and so on, providing scientifically valuable results. However, the preparation technology and use of BMGs still lag behind the

basic theoretical study. With regard to their applications, NASA (National Aeronautics and Space Administration) has assembled Zr-based bulk amorphous disks as detectors to collect solar wind [31], as well as explored the golf heads (hitting sites) [32].

The metastable structure of BMGs makes it difficult to process them by traditional welding and forging methods. Although BMGs exhibit an excellent superplastic forming ability, their supercooled liquid-phase region is extremely narrow. If the temperature is not appropriately controlled, crystallization can easily occur, leading to the performance deterioration of the amorphous alloy. Therefore, casting forming is one of the effective techniques to realize the engineering applications of BMGs. Since the mid-1990s, vacuum die casting has served for the fabrication of

BMGs. In particular, electronic casting method was developed by LiquidMetal Technologies based on the die-casting technology [33]. In 2016, RAMASAMY et al [34] applied high-pressure die casting (HPDC) to obtain Fe-based BMG key-shaped specimens. LIU et al [35,36] have proposed an approach called the “entire process vacuum high pressure die casting” (EPV-HPDC) and prepared a BMG smartphone frame as well as the BMG transmission successively used in a fabricated notebook computer. In 2016, HOFMANN et al [37] produced Zr- and Ti-based BMG flexsplines by suction casting. It is noteworthy that the thickness of amorphous alloy products prepared by the vacuum die-casting technology is within the range of 1–2 mm or even thinner. Therefore, it is still difficult to achieve the casting forming of large-sized BMGs with a kilogram-scale mass; hence, this technology cannot satisfy the requirements imposed to BMG structural parts for engineering applications. The problem is aggravated by the fact that there are a few studies reporting the casting forming of BMGs, though this topic is of theoretical and practical significance.

In the present study, an outer ring of 29320 spherical roller bearing was used in the casting forming of a $Zr_{41}Ti_{14}Cu_{12.5}Ni_{10}Be_{22.5}$ amorphous alloy. By conducting numerical simulations of mold filling and solidification during casting, the velocity distribution and flow behavior of the alloy melt in the mold were analyzed. Special attention was also paid to the temperature gradient, temperature field, and heat transfer rule of the alloy melt in mold filling and solidification processes. The combination of intermediate frequency induction melting and copper mold casting along with numerical simulation data enabled one to carefully investigate the gravity casting process of the outer ring of the 29320 spherical roller bearing and to develop the casting forming technology of BMGs.

2 Numerical simulation method

2.1 Establishment of mathematical model

Mold filling and solidification of castings are the sophisticated processes depending on various factors. Their simulation can be simplified using the following assumptions.

(1) The alloy melt is an incompressible Newtonian fluid.

(2) Because of the high mold filling speed and superheat, the alloy melt does not exhibit any phase change during mold filling.

(3) In the solidification process, the physical parameters of cast and mold materials are related to the temperature.

(4) The temperature of the inner surface of the mold is the same as that of the outer surface of the cast, and the heat-transfer process depends on the thermophysical properties of the mold and cast.

(5) Since the experiment is conducted in a closed vacuum environment, the mold boundary is set to be adiabatic.

2.1.1 Governing equations during mold filling

The flow of an alloy melt in mold filling during casting corresponds to the unsteady flow of an incompressible viscous liquid. Owing to the short filling time and the Reynolds coefficient greater than 2300, this flow is usually considered an underdeveloped turbulent flow; hence, the $k-\varepsilon$ model is used. The mold filling process includes momentum transfer, mass transfer, and energy transfer, and can thus be described by a set of the following equations [38,39].

(1) The continuity equation

$$\frac{\partial \rho}{\partial t} + \frac{\partial(\rho V_i)}{\partial i} = 0 \quad (1)$$

where V_i , ρ , t , and i represent the speed, density, time, and three-dimensional coordinates (x , y , z), respectively.

(2) The motion equation

$$\begin{aligned} \frac{\partial(\rho V_i)}{\partial t} + \frac{\partial(\rho V_x V_i)}{\partial x} + \frac{\partial(\rho V_y V_i)}{\partial y} + \frac{\partial(\rho V_z V_i)}{\partial z} = \\ \rho g_i - \frac{\partial P}{\partial i} + R_i + \frac{\partial}{\partial x}(\mu_e \frac{\partial V_i}{\partial x}) + \\ \frac{\partial}{\partial y}(\mu_e \frac{\partial V_i}{\partial y}) + \frac{\partial}{\partial z}(\mu_e \frac{\partial V_i}{\partial z}) \end{aligned} \quad (2)$$

where g , μ_e , P , and R are the gravitational acceleration, effective viscosity, pressure, and distributed resistance, respectively.

(3) The energy equation

$$\begin{aligned} \frac{\partial}{\partial t}(\rho c_p T) + \frac{\partial}{\partial x}(\rho V_x c_p T) + \\ \frac{\partial}{\partial y}(\rho V_y c_p T) + \frac{\partial}{\partial z}(\rho V_z c_p T) = \\ \frac{\partial}{\partial x}(\lambda \frac{\partial T}{\partial x}) + \frac{\partial}{\partial y}(\lambda \frac{\partial T}{\partial y}) + \frac{\partial}{\partial z}(\lambda \frac{\partial T}{\partial z}) + Q_V \end{aligned} \quad (3)$$

where c_p , T , λ , and Q_V are the specific heat capacity, temperature, thermal conductivity, and heat source, respectively.

2.1.2 Governing equations during solidification

In the present study, the nonlinear heat conduction finite element method is employed to perform specific calculations for the numerical simulation of casting solidification. The solidification process of the alloy melt involves the dissipation of heat to the environment through the mold. In this process, the internal temperature distribution of the casting and mold changes with time. From the perspective of heat-transfer approaches, heat transfer occurs via three routes: radiation, convection, and conduction. Clearly, radiation and convection mainly arise at the boundary. Assuming that the alloy melt does not undergo convection during solidification, the solidification of the casting can be basically regarded as an unstable heat conduction process. The basic mathematical model for the numerical simulation of casting solidification is the differential equation of unstable heat conduction. For a three-dimensional problem, the mathematical expression is as follows:

$$\rho c_p \frac{\partial T}{\partial t} = \frac{\partial}{\partial x} \left(\lambda \frac{\partial T}{\partial x} \right) + \frac{\partial}{\partial y} \left(\lambda \frac{\partial T}{\partial y} \right) + \frac{\partial}{\partial z} \left(\lambda \frac{\partial T}{\partial z} \right) + \rho Q \tag{4}$$

Here, the left-hand side of Eq. (4) represents the heat accumulation term, whereas the first three terms on the right-hand side rely on the heat conduction. Finally, the last term is associated with the latent heat. In addition to the initial and boundary conditions, solving Eq. (4) constitutes a mathematical model that describes the solidification of castings.

2.1.3 Thermophysical parameters of mold and amorphous alloy

Thermophysical parameters (such as thermal conductivity and specific heat capacity) and fluid parameters (such as viscosity, η) used herein are obtained from the previous studies [40–42]. Tables 1 and 2 show the parameters for the as-cast alloy and Cu mold, respectively.

2.2 Establishment of solid model

2.2.1 Modeling of gating system

Figure 1 shows the geometric dimensions of the outer ring of 29320 spherical roller bearing

(hereinafter referred to as ring-shaped cast). The casting system model for simulation analysis was established by building a seamless connection between Pro/E and ANSYS software. Figure 2

Table 1 Thermophysical properties of as-cast $Zr_{41}Ti_{14}Cu_{12.5}Ni_{10}Be_{22.5}$ amorphous alloy

$T/^\circ\text{C}$	$\rho/(\text{kg}\cdot\text{m}^{-3})$	$\lambda/(\text{W}\cdot\text{m}^{-1}\cdot^\circ\text{C}^{-1})$	$c_p/(\text{J}\cdot\text{kg}^{-1}\cdot^\circ\text{C}^{-1})$	$\eta/(\text{Pa}\cdot\text{s})$
0–350	6250	7.45	450	–
370	6250	8.3	530	$10^7\text{--}10^{11}$
390	6250	9.55	590	$10^7\text{--}10^{11}$
400–850	6250	10.28	643	–
850–1005	6250	10.28	643	0.001

Table 2 Thermophysical properties of Cu mold

$T/^\circ\text{C}$	$\rho/(\text{kg}\cdot\text{m}^{-3})$	$\lambda/(\text{W}\cdot\text{m}^{-1}\cdot^\circ\text{C}^{-1})$	$c_p/(\text{J}\cdot\text{kg}^{-1}\cdot^\circ\text{C}^{-1})$
20	8930	395	380
100	8900	392	399
300	8840	373	422
600	8740	344	456
900	8620	321	482

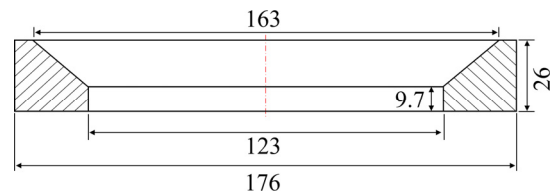


Fig. 1 Geometric dimensions of ring-shaped cast (unit: mm)

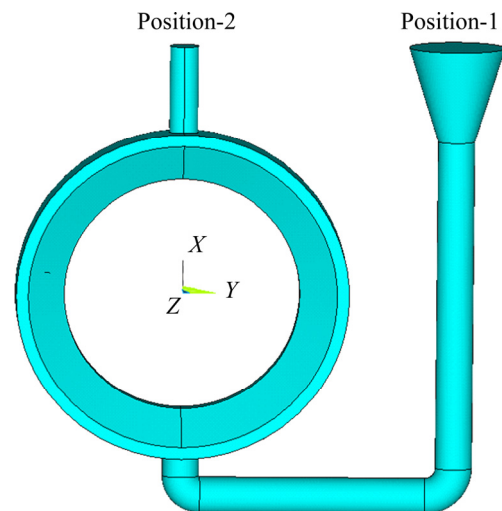


Fig. 2 Computational model of ring-shaped cast

shows the final computational model. Here, mold filling time refers to the time taken for the alloy melt to enter the mold (Position-1) and to reach the riser (Position-2). In turn, solidification time is the time taken for the alloy melt to cool to the equilibrium temperature after the mold filling is complete.

2.2.2 Determination of mold size

To attain the critical cooling rate during the casting of bulk amorphous alloys, it is imperative to select mold materials with good thermal conductivity and outstanding heat storage capacity. Owing to its high thermal conductivity, industrial pure copper is often used as a casting material. To achieve an appropriate critical cooling rate, the size of the copper mold needs to be evaluated based on the heat transfer (cooling rate) at the hot joint of the ring-shaped cast.

Figure 3 shows the simulated cooling curves of hotspots of casts in copper molds with different thicknesses. At the beginning of solidification, the cast exhibits an extremely high cooling rate. With the increase in the time to 50 s, the cooling capacity of the copper mold gradually decreases, and a plateau is observed. Table 3 shows the plateau temperature, average cooling rate, and instantaneous cooling rate at the glass transition temperature ($T_g=363\text{ }^\circ\text{C}$) of the casting hotspots. As can be seen from Table 3, with the increase in the thickness of the copper mold from 60 to 100 mm, the average cooling rate and instantaneous cooling rate at T_g significantly increase. When the mold thickness is greater than 100 mm, a marginal change is observed. The size of the mold used for simulations is $305\text{ mm} \times 305\text{ mm} \times 100\text{ mm}$.

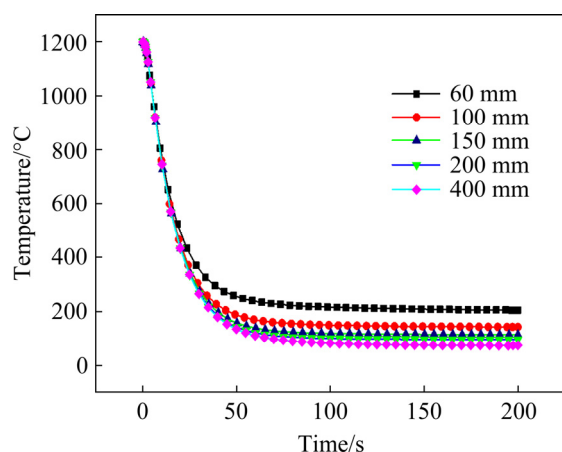


Fig. 3 Simulated cooling curves of hotspots of castings in copper molds with different thicknesses

Table 3 Parameters of hotspots of casts in copper molds with different thicknesses

Mold thickness/ mm	Plateau temperature/ °C	Average cooling rate/ (°C·s ⁻¹)	Instantaneous cooling rate/ (°C·s ⁻¹)
60	204.7	28.9	12.1
100	142.8	33.7	17.3
150	114	35	18
200	95.6	35.4	18.3
400	73.2	35.8	18.5

3 Numerical simulation of casting

3.1 Numerical simulation of mold filling

During the flow field simulation of mold filling, the filling speed at the inlet is 10 cm/s, the casting temperature is 1200 °C, and the initial temperature of the mold is 40 °C. Figure 4 shows the velocity fields for the mold filling of an alloy melt at different time. At the beginning of mold filling, the alloy melt rapidly flows into the mold cavity through the straight, horizontal, and inner runners. At the inlet of the inner runner of the mold, the alloy melt is divided into two strands, and it uniformly rises along the annular mold under the action of gravity, as indicated by the cyan streamline in Fig. 4(a). However, owing to the high temperature and rapid flow velocity of the alloy melt, large flow shocks (red and yellow streamlines) are observed at the turns of the straight, horizontal, and inner runners, as well as at the inlet of the inner runner. By increasing the mold filling time to 0.1 and 0.5 s (Figs. 4(b, c)), the fluidity of the alloy melt in the straight, horizontal, and inner runners is basically similar to that at a mold filling time of 0.01 s. However, uneven mold filling occurs, and the flow velocity of the left half ring is significantly greater than that of the right half ring. Pouring ends when the mold is filled for 1.8 s, and the alloy melt flows into the riser at the top of the cavity. With the decrease in the temperature, the alloy melt finally stops flowing (Fig. 4(d)).

Figure 5 displays the temperature fields of the cast at different time of the mold filling process. At a mold filling time of 0.01 s (Fig. 5(a)), the mold filling time is extremely short for the heat of the alloy melt to diffuse into the mold, even though the alloy melt rapidly flows into the cavity. In addition to the temperature distribution that can be observed at the sprue cup, the entire casting mold is basically

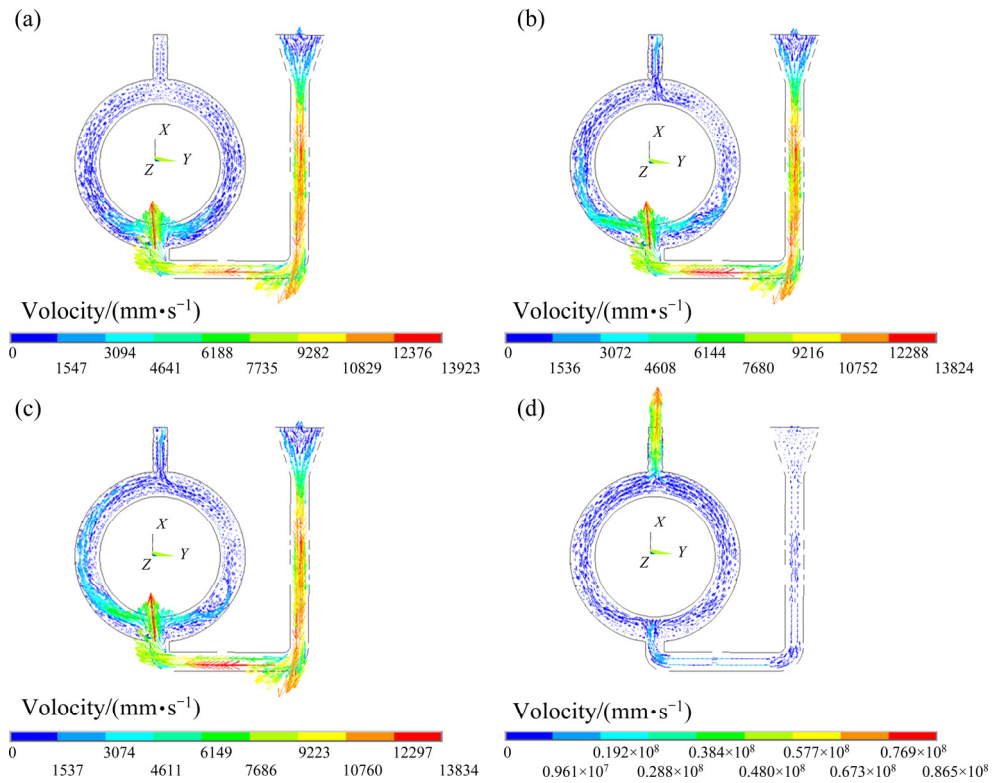


Fig. 4 Velocity fields of alloy melt at different time in mold filling: (a) 0.01 s; (b) 0.1 s; (c) 0.5 s; (d) 1.8 s

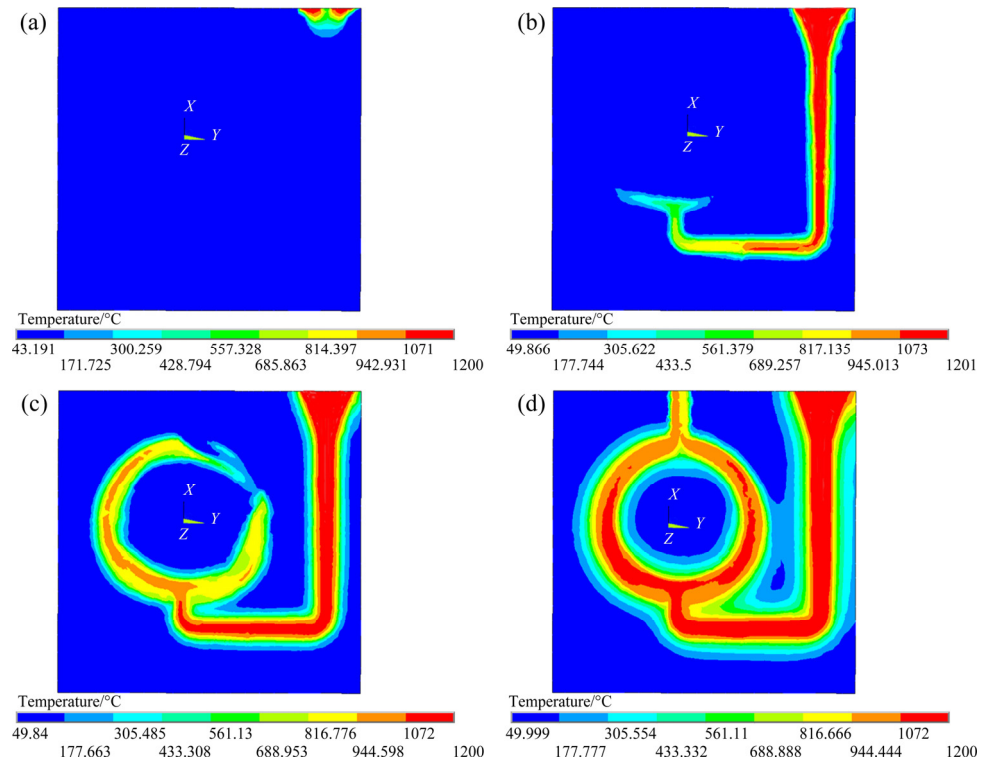


Fig. 5 Temperature fields in mold filling at different time: (a) 0.01 s; (b) 0.1 s; (c) 0.5 s; (d) 1.8 s

in the initial temperature state. At a mold filling time of up to 0.1 s (Fig. 5(b)), the heat of the alloy melt is transmitted to the mold surface through the

straight, horizontal, and inner runners, with the maximum heat transmitted from the straight runner. At a mold filling time of 0.5 s (Fig. 5(c)), the alloy

melt exhibits a relatively long heat conduction time, which can completely conduct heat through the mold. At the same time, the heat conduction on the left side of the ring-shaped cast is more rapid than that on the right side, which is in good agreement with the flow state shown in Fig. 4(c). At a mold filling time of 1.8 s (Fig. 5(d)), the mold is completely filled. As the alloy melt always maintains a high temperature in the straight, horizontal, and inner runners, as well as in the lower part of the ring-shaped cast, the latter exhibits a temperature distribution with the lowest temperature at the front end and the highest temperature at the sprue cup. As can be observed from the temperature field, at the completion of mold filling, the temperatures of the ring-shaped cast and gating system are greater than 1000 °C, whereas the temperature of the riser is between 816 and 940 °C. The found values are found to exceed the solidification temperature ($T_m=660$ °C) of the $Zr_{41}Ti_{14}Cu_{12.5}Ni_{10}Be_{22.5}$ amorphous alloy.

3.2 Numerical simulation of solidification

The temperature field of the mold and cast obtained after filling is utilized as the initial and boundary conditions for simulating the temperature field of solidification in an accurate manner. Figure 6 shows the temperature fields of the ring-

shaped cast at different time after the completion of filling. At a solidification time of 0.1 s (Fig. 6(a)), the temperatures of the ring-shaped cast and gating system slightly decrease, but the temperature in the central part is still greater than 900 °C, and the temperature in the central part of the riser is greater than 850 °C. At a solidification time of 10 s (Fig. 6(b)), the temperature of the sprue cup remains greater than 950 °C. The temperature in the central part of the ring-shaped cast ranges from 628 to 743 °C, while that of the remaining parts is reduced below 600 °C. The temperatures of the mold between the gating system and the cast and inside the ring-shaped profile cover a range between 170 and 280 °C. At a solidification time of 50 s (Fig. 6(c)), only the local temperature field on the left side of the annular cast is observed. The temperatures of the mold and cast go below 240 °C, except for an extremely small area near 300 °C at the upper right corner of the mold. At a casting solidification time of 100 s (Fig. 6(d)), except for a small area in the upper right corner, the temperatures of the cast and mold are found to be less than 200 °C. During solidification, the temperature of the mold increases from 46 to 162 °C, which is related to the heat transfer from the cast. According to the temperature field simulation, the temperature of the ring-shaped cast

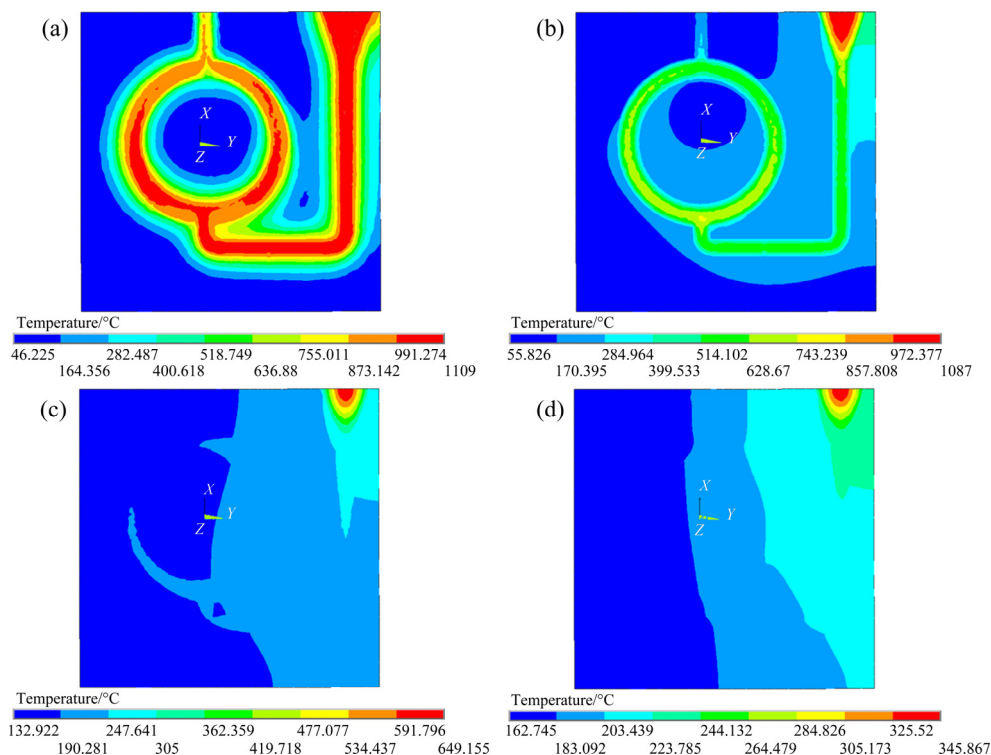


Fig. 6 Temperature fields at different time of solidification: (a) 0.1 s; (b) 10 s; (c) 50 s; (d) 100 s

at a solidification time of 50 s decreases from 1200 °C to the glass transition point ($T_g=363$ °C) of the $Zr_{41}Ti_{14}Cu_{12.5}Ni_{10}Be_{22.5}$ amorphous alloy. The average cooling rate of the ring-shaped part is ~ 17 °C/s, which is considerably greater than the critical cooling rate of the $Zr_{41}Ti_{14}Cu_{12.5}Ni_{10}Be_{22.5}$ amorphous alloys (1 °C/s) [1].

Figure 7 shows the temperature gradient fields in the course of solidification. According to the graphs from Fig. 6, the temperatures of the ring-shaped cast and mold are non-uniformly distributed, revealing a pronounced temperature gradient. During solidification, the strongest temperature gradient is observed at the interface between the cast and the mold (Fig. 7). With the heat transfer to the mold, the temperature distribution of the cast and the mold tends to be uniform. At the same time, the temperature gradient decreases to zero until the temperatures of the cast and mold become the same.

4 Casting forming of BMG

The size of the copper mold should satisfy the requirements for the heat-transfer capacity in solidification so that the alloy melt can be solidified at a cooling rate greater than the critical cooling rate of the amorphous alloy. During the solidification of

the ring-shaped cast, the heat of the alloy melt is absorbed and transferred through the copper mold. Generally, the heat release from casts during solidification is driven by conduction, convection, and radiation. As the casting of the Zr-based bulk amorphous alloy for ring-shaped parts is implemented in a vacuum smelting furnace in an argon atmosphere, convection and radiation heat-transfer capacities are extremely low, and cooling is mainly conducted via the heat storage capacity of the casting mold itself. The suitability of the mold size can be determined by the balance between the heat released by the alloy melt and the heat absorbed by the copper mold. The mass of the ring-shaped cast is 1.32 kg, but the alloy melt in the gating system needs to be considered for the heat balance calculation. Owing to the high viscosity of the Zr-based bulk amorphous alloy melt and the requirement for fast cooling, it is crucial to select a larger-sized gating system for rapid casting. In this study, the mass of the amorphous alloy (3.3 kg) used for the heat balance calculation is 1.5 times higher than that of the ring-shaped cast. The heat released by the alloy melt can be expressed as follows:

$$Q_r = m \int_{T_1}^{T_2} c_p dT \tag{5}$$

where m is the mass of the alloy melt, Q_r is the heat,

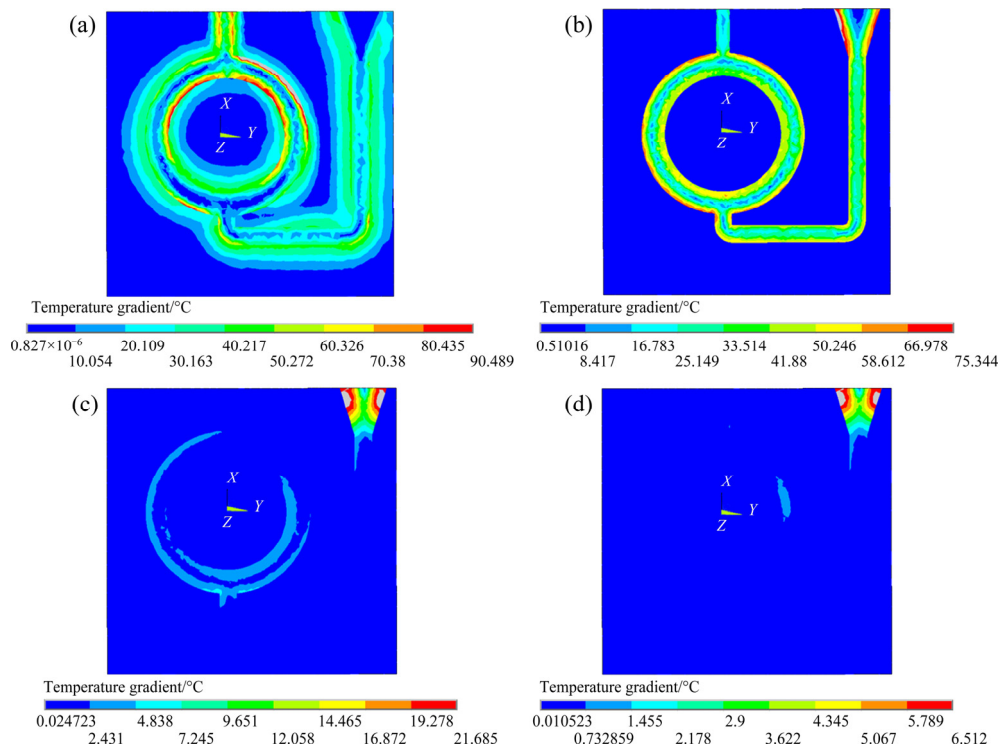


Fig. 7 Temperature gradient fields at different time of solidification: (a) 0.1 s; (b) 10 s; (c) 50 s; (d) 100 s

and T_1 and T_2 represent the temperatures. By substituting the parameters in Table 1 into Eq. (5), the heat released by the alloy melt from the casting temperature to the equilibrium temperature (200 °C) is confirmed to be -2012.67 kJ. To maintain heat balance, the heat released from the alloy melt should be equal to that absorbed by the copper mold. During casting, the temperature of the copper mold increases from room temperature to the equilibrium temperature, and the specific heat capacity of copper is 384 J/(kg·K); hence, the minimum required mass of the copper mold is 29 kg. In the actual casting experiment, the size and mass of the copper mold are 300 mm \times 260 mm \times 90 mm and 60 kg, respectively.

Figure 8 depicts the copper mold used for casting. The copper mold is divided into two parts, and the interface between the two parts is the parting surface. The bottom pouring system comprises straight, horizontal, and inner runners of equal diameters ($D=21$ mm), which can reduce the resistance of the alloy melt during mold filling.

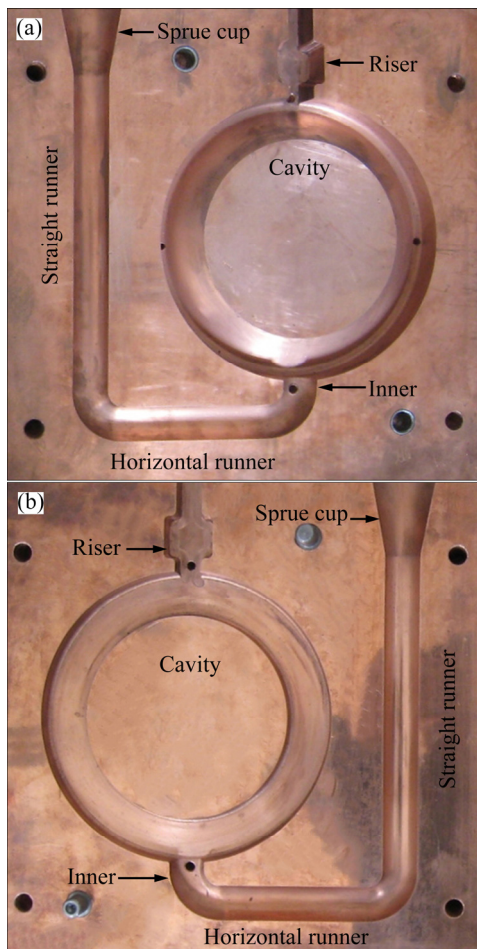


Fig. 8 Copper mold used for casting: (a) Left part; (b) Right part

Figure 9 shows the schematic diagram of the casting system. Table 4 lists the heating time at each power during heating. The casting temperature is measured through the observation hole using a hand-held dual colorimetric infrared thermometer, and the alloy melt is heated to 1200 °C for casting. The temperature change during filling and solidification is measured by a contact thermocouple placed at the riser.

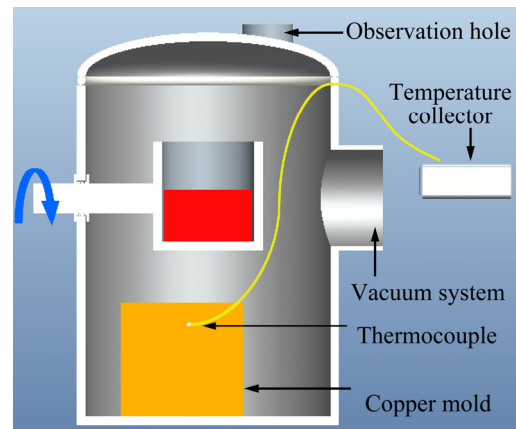


Fig. 9 Schematic diagram of casting system

Table 4 Power and time of heating process

Heating power/kW	2	10	30	40	50
Heating time/min	10	20	10	10	4

Figure 10 displays the ring-shaped part of the $Zr_{41}Ti_{14}Cu_{12.5}Ni_{10}Be_{22.5}$ amorphous alloy obtained by casting, as well as its X-ray diffraction (XRD) pattern and differential scanning calorimetry (DSC) curve. The ring-shaped part exhibits a smooth surface with a clear outline and well-formed shape (Fig. 10(a)). In the XRD pattern, the scattering peak near $2\theta=38.9^\circ$ is observed without any crystalline-phase-related diffraction reflexes, which is indicative of a typical amorphous structure of the cast. According to the DSC curve, the cast undergoes a glass transition, followed by the formation of a wide supercooled liquid region with a subsequent crystallization, as seen from the exothermic peaks.

5 Discussion

For traditional crystalline alloys, the alloy melt can maintain a long flow time due to the release of the latent heat of crystallization, thereby achieving

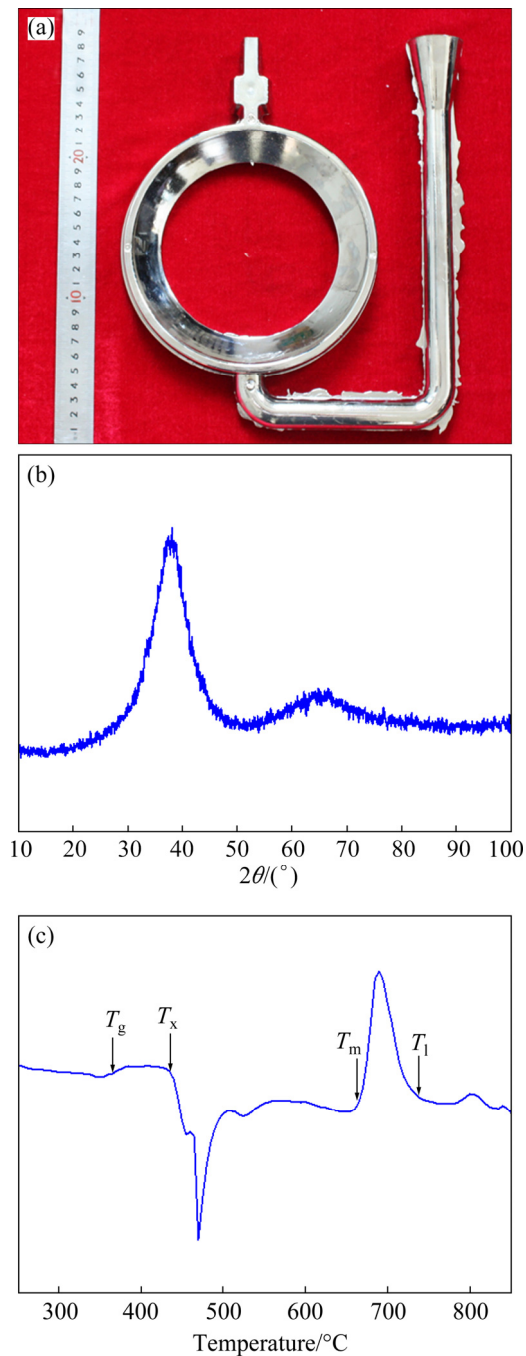


Fig. 10 Ring-shaped part (a), XRD pattern (b) and DSC curve (c) of $Zr_{41}Ti_{14}Cu_{12.5}Ni_{10}Be_{22.5}$ amorphous alloy

complete filling. However, in BMG casting, owing to the restriction of the amorphous forming ability, the alloy melt must be rapidly cooled under non-equilibrium solidification conditions, and the release of the latent heat of crystallization is not allowed to ensure the formation of an amorphous state. Therefore, the mold filling and solidification behavior of BMGs need to be explored and understood. Thus far, few studies have reported the

filling and solidification peculiarities of Zr-based BMG parts during casting. In this respect, the combination of numerical simulations and experimental study would allow one to elucidate the filling and solidification stages of large-sized Zr-based BMG units in the course of casting.

5.1 Mold filling process

Figure 11 displays the experimentally measured and simulated temperatures at the riser as functions of time during filling. At a filling time of less than 1.14 s, the measured temperature fluctuates between 30 and 40 °C, indicating that the alloy melt does not completely fill the cavity at this time. At a filling time of 1.47 s, the experimental temperature rapidly increases, meaning that the alloy melt reaches the top of the casting and enters in contact with the thermocouple. At this time, the tested temperature reaches 859 °C, which is within a range of 816–944 °C at the end of the simulated mold filling process (Fig. 5). From the simulated curve, the time for the alloy melt to reach the top of the cast is 1.76 s, and the corresponding temperature is 900 °C, which is similar to the experimental result. The flow behavior of the Zr-based bulk amorphous alloy melt during filling can be explained in terms of the simulated temperature field during mold filling. At the initial stage of mold filling (0.1 s), a small amount of the high-temperature alloy melt reaches the bottom of the cavity through the gating system. However, owing to the relatively low content of the alloy melt and the strong cooling capacity of the copper mold, the temperature at the front end of the alloy melt rapidly decreases to ~400 °C. With the continuation of mold filling, the subsequent alloy melts by heat conduction, thereby increasing the temperature of the alloy melt at the front end, so that it can continue to flow until the cavity is completely filled. At the end of filling, the temperature of the riser in the cast is 859 °C, which is 341 °C lower than the casting temperature (1200 °C). In the copper mold casting of the amorphous alloy, the rapid pouring process at high temperatures must be utilized to make the alloy melt maintain the superheat (>600 °C) for mold filling. This enables one to overcome the difficulties associated with high viscosity of the amorphous alloy melt and large cooling capacity of the copper mold, as well as to ensure the clear outline and complete shape of the cast.

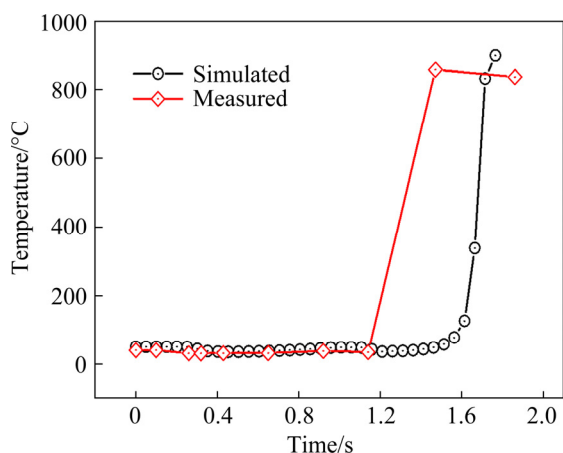


Fig. 11 Experimental and simulated temperatures at riser as function of time during mold filling process

5.2 Solidification process

Figure 12 shows simulated and experimental cooling curves of the $Zr_{41}Ti_{14}Cu_{12.5}Ni_{10}Be_{22.5}$ amorphous alloy melt during solidification. The two cooling curves exhibit the same variation trend, indicating the coincidence between the simulated and measured solidification cooling rates of the alloy melt. At the initial stage of solidification, the temperature of the alloy melt rapidly decreases, but the slope of the experimental cooling curve is slightly greater than that of the simulated one, meaning that the measured cooling rate slightly exceeds the value obtained by simulation. At a solidification time of ~ 10 s, the temperature of the alloy melt decreases to near T_g (363 °C), and the average cooling rate is ~ 50 °C/s, which is considerably higher than the critical cooling rate of the $Zr_{41}Ti_{14}Cu_{12.5}Ni_{10}Be_{22.5}$ amorphous alloy (1 °C/s). At a solidification time of 50 s, the

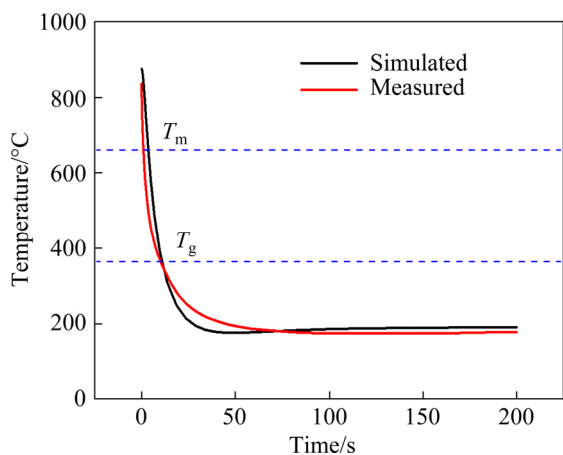


Fig. 12 Simulated and measured cooling curves during solidification process

average cooling rate is ~ 15.3 °C/s, which is still greater than the critical cooling rate of $Zr_{41}Ti_{14}Cu_{12.5}Ni_{10}Be_{22.5}$ amorphous alloys. With a further increase in the solidification time to 64 s, the simulated and experimental cooling curves intersect at 185 °C, and then remain unchanged.

6 Conclusions

(1) According to numerical simulations of the mold filling of a Zr-based bulk amorphous alloy melt, the temperatures of the ring-shaped cast and the gating system at the completion of the process were greater than 1000 °C, whereas the temperature of the riser was between 816 and 940 °C. These temperatures exceeded the point of solidification ($T_m=660$ °C) of $Zr_{41}Ti_{14}Cu_{12.5}Ni_{10}Be_{22.5}$ amorphous alloy. Therefore, rapid casting can overcome the viscous obstruction caused by the high viscosity of the amorphous alloy and satisfy the requirements for the mold filling capacity during casting process.

(2) According to the numerical simulation of solidification, at a solidification time of 50 s, the temperature of the ring-shaped part dropped from the casting value (1200 °C) to the glass transition point ($T_g=363$ °C) of the $Zr_{41}Ti_{14}Cu_{12.5}Ni_{10}Be_{22.5}$ amorphous alloy, and the average cooling rate at that moment was ~ 17 °C/s. The measured cooling curve during solidification indicates that, at the same time of 50 s, the average cooling rate is ~ 15.3 °C/s, being higher than the critical cooling rate of the $Zr_{41}Ti_{14}Cu_{12.5}Ni_{10}Be_{22.5}$ amorphous alloy (1 °C/s).

(3) Based on the numerical simulation of mold filling and solidification, a large-sized $Zr_{41}Ti_{14}Cu_{12.5}Ni_{10}Be_{22.5}$ BMG ring-shaped part with a mass of 1.32 kg was prepared by casting.

Acknowledgments

This work was financially supported by the National Natural Science Foundation of China (Nos. 52071278, 51827801), the National Key Research and Development Program of China (No. 2018YFA0703603), and the Hebei Normal University of Science & Technology, China (No. 2021YB012).

References

- [1] PEKER A, JOHNSON W L. A highly processable metallic glass: $Zr_{41.2}Ti_{13.8}Cu_{12.5}Ni_{10.0}Be_{22.5}$ [J]. Applied Physics

- Letters, 1993, 63(17): 2342–2344.
- [2] CHEN W, WANG Y, QIANG J, DONG C. Bulk metallic glasses in the Zr–Al–Ni–Cu system [J]. *Acta Materialia*, 2003, 51(7): 1899–1907.
- [3] YU De-chuan, SHI Xiao-gang, FU Hua-meng, GENG Yan, ZHU Zheng-wang, QI Yang, ZHANG Hai-feng. Glass formation in Zr–Al–Fe–Cu system [J]. *Materials Letters*, 2015, 157: 299–302.
- [4] INOUE A, NISHIYAMA N, KIMURA H. Preparation and thermal stability of bulk amorphous Pd₄₀Cu₃₀Ni₁₀P₂₀ alloy cylinder of 72 mm in diameter [J]. *Materials Transactions JIM*, 1997, 38(2): 179–183.
- [5] LÖFFLER J F, SCHROERS J, JOHNSON W L. Time–temperature–transformation diagram and microstructures of bulk glass forming Pd₄₀Cu₃₀Ni₁₀P₂₀ [J]. *Applied Physics Letters*, 2000, 77(5): 681–683.
- [6] WANG Qing, DONG Chuang, QIANG Jian-bing, WANG Ying-min. Cluster line criterion and Cu–Zr–Al bulk metallic glass formation [J]. *Materials Science and Engineering A*, 2007, 449–451: 18–23.
- [7] HUI X, DONG W, CHEN G L, YAO K F. Formation, microstructure and properties of long-period order structure reinforced Mg-based bulk metallic glass composites [J]. *Acta Materialia*, 2007, 55(3): 907–920.
- [8] YAN M, ZOU J, SHEN J. Cooling rate effects on the microstructure and phase formation in Zr₅₁Cu_{20.7}Ni₁₂Al_{16.3} bulk metallic glass [J]. *Science and Technology of Advanced Materials*, 2006, 7(8): 806–811.
- [9] MOHAMMADI RAHVARD M, TAMIZIFAR M, ALIBOUTORABI S M. Zr–Co(Cu)–Al bulk metallic glasses with optimal glass-forming ability and their compressive properties [J]. *Transactions of Nonferrous Metals Society of China*, 2018, 28(8): 1543–1552.
- [10] FÁTAY D, GUBICZA J, SZOMMER P, LENDVAI J, BLÉTRY M, GUYOT P. Thermal stability and mechanical properties of a Zr-based bulk amorphous alloy [J]. *Materials Science and Engineering A*, 2004, 387–389: 1001–1004.
- [11] INOUE A, TAKEUCHI A. Recent progress in bulk glassy, nanoquasicrystalline and nanocrystalline alloys [J]. *Materials Science and Engineering A*, 2004, 375: 16–30.
- [12] LIU L, CHAN K C, SUN M, CHEN Q. The effect of the addition of Ta on the structure, crystallization and mechanical properties of Zr–Cu–Ni–Al–Ta bulk metallic glasses [J]. *Materials Science and Engineering A*, 2007, 445/446: 697–706.
- [13] MINOUEI H, AKBARI G H, ENAYATI M H, HONG S I. Non-isothermal nano-crystallization kinetics in amorphous Ni₅₅Nb₃₅Si₁₀ alloy [J]. *Transactions of Nonferrous Metals Society of China*, 2019, 29(2): 358–364.
- [14] WANG Wei-hua. The elastic properties, elastic models and elastic perspectives of metallic glasses [J]. *Progress in Materials Science*, 2012, 57(3): 487–656.
- [15] BIAN Z, HE G, CHEN G L. Investigation of shear bands under compressive testing for Zr-base bulk metallic glasses containing nanocrystals [J]. *Scripta Materialia*, 2002, 46(6): 407–412.
- [16] GU Ji, ZHANG Li-xin, WANG Yi-han, NI Song, GUO Sheng-feng, SONG Min. Combined effect of isothermal annealing and pre-compression on mechanical properties of Cu₃₆Zr₄₈Al₈Ag₈ bulk metallic glass [J]. *Transactions of Nonferrous Metals Society of China*, 2016, 26(6): 1620–1628.
- [17] KOZIEL T, PAJOR K, CIOS G, BAŁA P. Effect of strain rate and crystalline inclusions on mechanical properties of bulk glassy and partially crystallized Zr_{52.5}Cu_{17.9}Ni_{14.6}Al₁₀Ti₅ alloy [J]. *Transactions of Nonferrous Metals Society of China*, 2019, 29(5): 1036–1045.
- [18] ZHANG Z F, HE G, ECKERT J, SCHULTZ L. Fracture mechanisms in bulk metallic glassy materials [J]. *Physical Review Letters*, 2003, 91(4): 045505.
- [19] WANG W H, DONG C, SHEK C H. Bulk metallic glasses [J]. *Materials Science and Engineering R: Reports*, 2004, 44(2/3): 45–89.
- [20] XI X K, ZHAO D Q, PAN M X, WANG W H, WU Y, LEWANDOWSKI J J. Fracture of brittle metallic glasses: Brittleness or plasticity [J]. *Physical Review Letters*, 2005, 94(12): 125510.
- [21] ZHANG G Q, JIANG Q K, CHEN L Y, SHAO M, LIU J F, JIANG J Z. Synthesis of centimeter-size Ag-doped Zr–Cu–Al metallic glasses with large plasticity [J]. *Journal of Alloys and Compounds*, 2006, 424(1/2): 176–178.
- [22] LIU Yan-hui, WANG Gang, WANG Ru-ju, ZHAO De-qian, PAN Ming-xiang, WANG Wei-hua. Super plastic bulk metallic glasses at room temperature [J]. *Science*, 2007, 315(5817): 1385–1388.
- [23] ZHANG Y, WANG W H, GREER A L. Making metallic glasses plastic by control of residual stress [J]. *Nature Materials*, 2006, 5(11): 857–860.
- [24] MA D Q, JIAO W T, ZHANG Y F, WANG B A, LI J, ZHANG X Y, MA M Z, LIU R P. Strong work-hardening behavior induced by the solid solution strengthening of dendrites in TiZr-based bulk metallic glass matrix composites [J]. *Journal of Alloys and Compounds*, 2015, 624: 9–16.
- [25] MA D Q, LI J, ZHANG Y F, ZHANG X Y, MA M Z, LIU R P. Effect of compositional tailoring on the glass-forming ability and mechanical properties of TiZr-based bulk metallic glass matrix composites [J]. *Materials Science and Engineering A*, 2014, 612: 310–315.
- [26] WU Hong, XU Feng, REN Jun-ye, LAN Xiao-dong, YIN Yong, LIANG Lu-xin, SONG Min, LIU Yong, LI Jia, LI Qing-xiang, HUANG Wei-dong. Rate-dependent inhomogeneous creep behavior in metallic glasses [J]. *Transactions of Nonferrous Metals Society of China*, 2021, 31(6): 1758–1765.
- [27] ZHONG H, CHEN J, DAI L Y, YUE Y, WANG B A, ZHANG X Y, MA M Z, LIU R P. Effect of counterpart material on the tribological properties of Zr-based bulk metallic glass under relatively heavy loads [J]. *Wear*, 2016, 346: 22–28.
- [28] ZHONG Hua, CHEN Jun, DAI Luan-yue, YUE Yue, ZHANG Zhi-wei, ZHANG Xin-yu, MA Ming-zhen, LIU Ri-ping. Tribological behaviors of Zr-based bulk metallic glass versus Zr-based bulk metallic glass under relative heavy loads [J]. *Intermetallics*, 2015, 65: 88–93.
- [29] WU Hong, LAN Xiao-dong, LIU Yong, LI Fei, ZHANG Wei-dong, CHEN Zi-jin, ZAI Xiong-fei, ZENG Han.

- Fabrication, tribological and corrosion behaviors of detonation gun sprayed Fe-based metallic glass coating [J]. Transactions of Nonferrous Metals Society of China, 2016, 26(6): 1629–1637.
- [30] YUE Y, WANG R, MA D Q, TIAN J F, ZHANG X Y, JING Q, MA M Z, LIU R P. Fatigue behavior of a Zr-based bulk metallic glass under uniaxial tension–tension and three-point bending loading mode [J]. Intermetallics, 2015, 60: 86–91.
- [31] TELFORD M. The case for bulk metallic glass [J]. Materials Today, 2004, 7(3): 36–43.
- [32] KAKIUCHI H, INOUE A, ONUKI M, TAKANO Y, YAMAGUCHI T. Application of Zr-based bulk glassy alloys to golf clubs [J]. Materials Transactions, 2001, 42(4): 678–681.
- [33] HOFMANN D C, ROBERTS S N. Microgravity metal processing: from undercooled liquids to bulk metallic glasses [J]. NPJ Microgravity, 2015, 1(1): 15003.
- [34] RAMASAMY P, SZABO A, BORZEL S, ECKERT J, STOICA M, BÁRDOS A. High pressure die casting of Fe-based metallic glass [J]. Scientific Reports, 2016, 6(1): 35258.
- [35] LIU L H, ZHANG T, LIU Z Y, YU C Y, DONG X X, HE L J, GAO K, ZHU X G, LI W H, WANG C Y, LI P J, ZHANG L C, LI L. Near-net forming complex shaped Zr-based bulk metallic glasses by high pressure die casting [J]. Materials, 2018, 11(11): 2338.
- [36] LIU L H, ZHANG T, LIU Z Y, WANG C Y, HE L J, LI P J, LI W R, LI L. Abnormal increase of glass forming ability under rising mold temperature in high pressure die casting [J]. Materials Letters, 2019, 247: 215–218.
- [37] HOFMANN D C, POLIT-CASILLAS R, ROBERTS S N, BORGONIA J P, DILLON R P, HILGEMANN E, KOLODZIEJSKA J, MONTEMAYOR L, SUH J O, HOFF A, CARPENTER K, PARNES A, JOHNSON W L, KENNETT A, WILCOX B. Castable bulk metallic glass strain wave gears: Towards decreasing the cost of high-performance robotics [J]. Scientific Reports, 2016, 6(1): 37773.
- [38] HUERTA A, LIU W K. Viscous flow with large free surface motion [J]. Computer Methods in Applied Mechanics and Engineering, 1988, 69(3): 277–324.
- [39] YOU Dong-dong, SHAO Ming, LI Yuan-yuan, ZHOU Zhao-yao. Numerical simulation of mold-temperature-control solidification [J]. Transactions of Nonferrous Metals Society of China, 2007, 17(3): 443–448.
- [40] XU Dong-hua, JOHNSON W L. Crystallization kinetics and glass-forming ability of bulk metallic glasses Pd₄₀Cu₃₀-Ni₁₀P₂₀ and Zr_{41.2}Ti_{13.8}Cu_{12.5}Ni₁₀Be_{22.5} from classical theory [J]. Physical Review B, 2006, 74(2): 024207.
- [41] MUKHERJEE S, SCHROERS J, JOHNSON W L, RHIM W K. Influence of kinetic and thermodynamic factors on the glass-forming ability of zirconium-based bulk amorphous alloys [J]. Physical Review Letters, 2005, 94(24): 245501.
- [42] MUKHERJEE S, SCHROERS J, ZHOU Z, JOHNSON W L, RHIM W K. Viscosity and specific volume of bulk metallic glass-forming alloys and their correlation with glass forming ability [J]. Acta Materialia, 2004, 52(12): 3689–3695.

大尺寸 Zr 基块体金属玻璃环形件铸造过程的数值模拟及实验验证

王飞龙¹, 郝秋红^{1,2}, 于鹏飞¹, 杨玉婧³, 马明臻¹, 张新宇¹, 刘日平¹

1. 燕山大学 亚稳材料制备技术与科学国家重点实验室, 秦皇岛 066004;

2. 武汉华工赛百数据系统有限公司, 武汉 430223;

3. 河北科技师范学院 物理系, 秦皇岛 066004

摘要: 以 29320 调心滚子轴承外圈为研究对象, 对 Zr₄₁Ti₁₄Cu_{12.5}Ni₁₀Be_{22.5} 非晶合金的铸造成形进行实验研究。通过对充型和凝固过程的数值模拟, 得到合金熔体在充型过程中的速度场和温度场, 以及凝固过程中的温度场和温度梯度场。结果表明, 当浇铸温度为 1200 °C 时, 能以大于临界冷速率的冷却速率获得外形完整的铸件。采用重力铸造方法在铜铸型模具中制备厚度为 25 mm、当量直径为 22 mm 和质量为 1.32 kg 的环形件。X 射线衍射和差示扫描量热分析结果表明铸件为非晶态结构。

关键词: 块体金属玻璃; 环形件; 铸造成形; 数值模拟; 充型; 凝固

(Edited by Wei-ping CHEN)